



RESEARCH LETTER

10.1002/2017GL076177

Key Points:

- From quenched dendritic textures, estimated ferropericlase melt viscosity near melting temperature is 10^{-3} – 10^{-2} Pa·s between 3–70 GPa
- Present experimental results for ferropericlase melt viscosity are consistent with previous computational results
- The low viscosity of ferropericlase melt implies vigorous convection and fast cooling of an early magma ocean

Supporting Information:

- Supporting Information S1

Correspondence to:

Z. Du,
zdu@carnegiescience.edu

Citation:

Du, Z., Deng, J., & Lee, K. K. M. (2017). Experimental constraints on ferropericlase (Mg, Fe)O melt viscosity up to 70 GPa. *Geophysical Research Letters*, 44. <https://doi.org/10.1002/2017GL076177>

Received 26 OCT 2017

Accepted 9 DEC 2017

Accepted article online 15 DEC 2017

Experimental Constraints on Ferropericlase (Mg, Fe) O Melt Viscosity Up to 70 GPa

Zhixue Du^{1,2} , Jie Deng¹ , and Kanani K. M. Lee¹ 

¹Department of Geology and Geophysics, Yale University, New Haven, CT, USA, ²Now at Geophysical Laboratory, Carnegie Institution of Washington, Washington, DC, USA

Abstract During Earth's accretion, Earth's mantle is expected to have been a magma ocean due to large impacts. As such, properties of molten mantle materials are key to understanding Earth's thermochemical evolution. However, due to experimental challenges, transport properties at lower mantle pressures, particularly viscosity, are poorly constrained for mantle melts. In this study, we use quenched dendritic textures to estimate melt viscosities at high pressures for (Mg, Fe)O ferropericlase, one of the major components of the mantle. We find that the viscosity of (Mg, Fe)O melt near liquidus temperatures is $\sim 10^{-3}$ – 10^{-2} Pa s over the pressure range of 3–70 GPa, which is ~ 1 – 2 orders of magnitude lower than previous results for Si-rich melts at similar conditions. This may have implications for magma ocean cooling and thermochemical evolution of the mantle.

1. Introduction

An early, deep magma ocean on Earth has been hypothesized to explain the mantle's moderately siderophile element abundances (e.g., Li & Agee, 1996; Rubie et al., 2011), as well as a likely outcome after the energetic Moon-forming giant impact (e.g., Canup, 2004; Cuk & Stewart, 2012). Understanding the subsequent evolution of the magma ocean is crucial to unfold the nature and evolution of Earth's early atmosphere, tectonics, and mantle geochemistry (e.g., Elkins-Tanton, 2012; Wood et al., 2006). Therefore, material properties of silicate/oxide liquids, particularly transport properties (e.g., viscosity), are of primary importance to understand the convection style, cooling, and crystallization of a deep magma ocean (e.g., Karki & Stixrude, 2010; Solomatov & Stevenson, 1993).

Ferropericlase (Mg, Fe)O is one of the main components of the mantle; however, the viscosity of this melt at high pressures has not been examined due to technical difficulties. That is, the extreme temperatures required to melt (Mg, Fe)O at high pressures (Du & Lee, 2014; Deng & Lee, 2017) render the conventional methods of measuring melt viscosity difficult (e.g., falling sphere viscometry; Kanzaki et al., 1987). Furthermore, experimental results on other mantle compositions have been limited to lower pressures, for example, enstatite melt up to 8 GPa (Cochain et al., 2017), fayalite melt up to 9 GPa (Spice et al., 2015), and peridotite melt up to 13 GPa (Dingwell et al., 2004; Liebske et al., 2005). Computational studies have covered the Mg end-member compositions MgO, MgSiO₃, and Mg₂SiO₄ up to core-mantle boundary (CMB) conditions (Adjaoud et al., 2011; Alfe, 2005; Karki, 2015; Karki & Stixrude, 2010). Recently, the total self-diffusivity of (Mg_{0.75}, Fe_{0.25})O has also been computed (Holmstrom & Stixrude, 2016), although the viscosity of the same material is still lacking.

In this study, we propose a novel method to estimate viscosity of (Mg, Fe)O melt at high pressures using the Eyring relation, where self-diffusivity is determined from quenched textures. Our experimental estimates are in good agreement with molecular dynamic density functional theory results (Alfe, 2005; Karki, 2015).

2. Materials and Methods

We performed a set of high-pressure melting experiments for (Mg_{1-x}, Fe_x)O ($x = 0.1, 0.2$) using a laser-heated diamond anvil cell, with experimental details described in a previous study (Du & Lee, 2014). We compile the experimental results from Du and Lee (2014) and Deng et al. (2017), with temperature corrections due to wavelength-dependent absorption (Deng et al., 2017). All symbols, experimental conditions, and results are summarized in Tables 1–3, respectively.

For liquids, the Eyring relation relates dynamic viscosity (η) and element self-diffusivity (D) (Eyring, 1936):

Table 1
 Definition of Symbols in the Text

Symbol	Definition
D	Solute diffusion coefficient
σ_D	Error of D , solute diffusion coefficient
η	Dynamic viscosity
k_B	Boltzmann constant: $1.38 \times 10^{-23} \text{ m}^2 \text{ kg s}^{-2} \text{ K}^{-1}$
λ	Elementary diffusion step, Fe or Mg in this study
T	Melt temperature
R_d	Hydrodynamic radius of diffusion species, for example, Mg, Fe, and O
κ_m	Thermal diffusivity of (Mg, Fe)O melt
d	Grain size of quenched crystal
L_m	Thickness of melt layer
L_t	Thickness of top insulation layer
L_b	Thickness of bottom insulation layer
τ	Dendrites growth time
$\tau_m \sim (L_m)^2/\kappa_m$	Thermal diffusion time for melt layer to cool
Γ	Gibbs-Thomson coefficient
λ_1	Primary dendritic arm spacing
k	Solute partition coefficient
T_L	Liquidus temperature
ΔT	The difference between liquidus and solidus equilibrium temperature
$V \sim L_m/\tau_m$	Tip velocity
$G \sim \Delta T/L_m$	Temperature gradient in front of the liquidus isotherm
$P_{\text{post-heating}}$	Pressure measured after melting

$$D\eta = k_B T / \lambda \quad (1)$$

where k_B is Boltzmann constant, T is melt temperature, and λ is the elementary diffusion step. Note that this becomes the Stokes-Einstein equation when $\lambda = \alpha\pi R_d$, where R_d is the hydrodynamic radius of the diffusion species ($R_d = 0.77 \text{ \AA}$ for high-spin Fe^{2+} and 0.72 \AA for Mg^{2+} ; Shannon & Prewitt, 1969) and α is a constant ranging between ~ 4 and 6 depending on the boundary conditions (Adjaoud et al., 2011). λ is assumed to be 11 \AA for all of our experimental pressures, which is the minimum value indicated by previous computational results (Adjaoud et al., 2011; Ghosh & Karki, 2011); therefore, $\alpha = 4.5$ for Fe^{2+} and 4.9 for Mg^{2+} . Choosing a larger value for λ will further decrease the estimates of viscosity in this study. Using a smaller R_d for the diffusion species (e.g., $R_d = 0.61 \text{ \AA}$ for low-spin Fe^{2+}) will increase α for Fe^{2+} ; however, it will still be within the range of 4 – 6 .

Table 2
 Summary of Spatial Measurements and Temporal Estimates

Experiment run no.	λ_1 (μm)	L_m (μm)	τ (μs)	κ_m (mm^2/s) ^a	V (m/s)	L_t (μm)	L_b (μm)
14-0409-91	0.45(5)	3.2(1)	9.3	1.1(2)	0.34	3.0(2)	16.9(1)
14-0506_3G	0.27(4)	1.6(2)	2.3	1.1(2)	0.70	2.0(3)	19.2(5)
14-0416	0.52(8)	2.4(2)	5.2	1.1(2)	0.45	2.6(3)	18.8(2)
13-1118	0.55(9)	2.4(1)	5.2	1.1(2)	0.45	2.5(2)	17.1(3)
15-0326R2D2	0.86(5)	4.3(3)	16.8	1.1(2)	0.26	3.3(3)	31.0(2)
15-0326Y02	0.77(2)	2.5(1)	6.3	1.1(2)	0.40	4.7(1)	26.6(2)
13-0814	0.47(10)	2.2(1)	3.2	1.5(2)	0.69	1.0(1)	14.3(2)
14-0610	0.58(10)	2.1(1)	4.4	1.0(1)	0.48	2.5(2)	13.8(2)
14-0506_45G	0.45(3)	2.0(1)	3.3	1.2(1)	0.61	0.8(1)	14.8(2)
14-0426	0.47(5)	2.0(1)	4.4	0.9(1)	0.45	1.2(1)	14.8(2)
May2915	0.42(5)	2.2(2)	2.0	2.4(2)	1.0	0.98(5)	11.1(2)
Jul0415	NA	1.9(1)	1.7	2.2(2)	NA	1.9(1)	10.1(3)
13-1009	NA	0.5(1)	0.7 ^b	2.1(3)	NA	0.60(4)	8.8(1)

Note. The 1σ errors are given for the last significant digit in parentheses. If not applicable, NA is recorded.

^aAssumed to be the same as MgO solid at the melting point, taken from (Stackhouse et al., 2010). ^bThe value $0.7 \mu\text{s}$ is the laser modulation fall time.

Table 3
Summary of Experimental Conditions and Calculated Dynamical Parameters

Experiment run no.	$P_{\text{post-heating}}$ (GPa)	T_L^a (K)	Starting material, Mg#	Melt (Mg#)	k	ΔT (K)	Γ (10^{-7} K m)	G (10^9 K/m)	D (10^{-8} m ² /s)	σ_D (factor)	η (mPa s)
14-0409-91	3(1)	2830(250)	91(1)	72(2)	0.27(9)	761	2.7(2)	0.24(1)	0.30	2.9	11.7
14-0506_3G	3(1)	2550(250)	81(1)	43(2)	0.43(18)	711	2.4(2)	0.44(5)	0.53	4.2	6.0
14-0416	11(1)	3430(300)	91(1)	75(2)	0.32(7)	573	3.2(3)	0.24(2)	0.96	3.6	4.5
13-1118	11(1)	3100(300)	79(1)	58(2)	0.41(12)	584	2.9(3)	0.24(1)	1.7	4.4	2.3
15-0326R2D2	10(1)	3150(300)	90(1)	70(1)	0.23(1)	428	2.9(3)	0.10(1)	1.5	1.9	3.1
15-0326Y02	10(1)	3250(300)	89(1)	75(1)	0.18(11)	410	3.0(3)	0.15(1)	3.3	2.4	1.3
13-0814	27(1)	3790(350)	91(1)	74(2)	0.24(12)	1055	3.4(3)	0.48(2)	1.9	5.2	2.9
14-0610	27(1)	3450(350)	91(1)	68(2)	0.28(14)	1011	3.1(3)	0.48(2)	2.0	4.5	2.4
14-0506_45G	38(1)	4400(450)	91(1)	67(2)	0.27(15)	1488	3.9(4)	0.74(4)	0.68	3.6	5.8
14-0426	40(1)	3910(350)	91(1)	55(2)	0.35(18)	1261	3.5(4)	0.63(3)	1.6	3.4	2.6
May2915	66(1)	3650(350)	88(1)	67(5)	0.25(2)	902	3.1(3)	0.41(2)	1.4	3.0	3.3
Jul0415	60(1)	3270(300)	81(1)	59(1)	$d(\mu\text{m}): 0.14(2)$				1.2	2.0	3.4
13-1009	70(1)	3100(250)	81(1)	$<40^b$	$d(\mu\text{m}): 0.12(2)$				2.0	2.6	1.9

Note. The 1σ errors are given on the last significant digit in parentheses or separate columns.

^aTemperatures (Du & Lee, 2014) have been corrected due to wavelength-dependent absorption that plagues (Mg, Fe)O samples based on inverse modeling in a previous study (Deng et al., 2017). ^bThe thickness of the melt layer is $0.6 \mu\text{m}$, smaller than the $\sim 1 \mu\text{m}$ spatial resolution of electron microprobe (Du & Lee, 2014). Therefore, our measurements are taken as an upper bound as the electron beam probes not only the melt layer but also the coexisting solid.

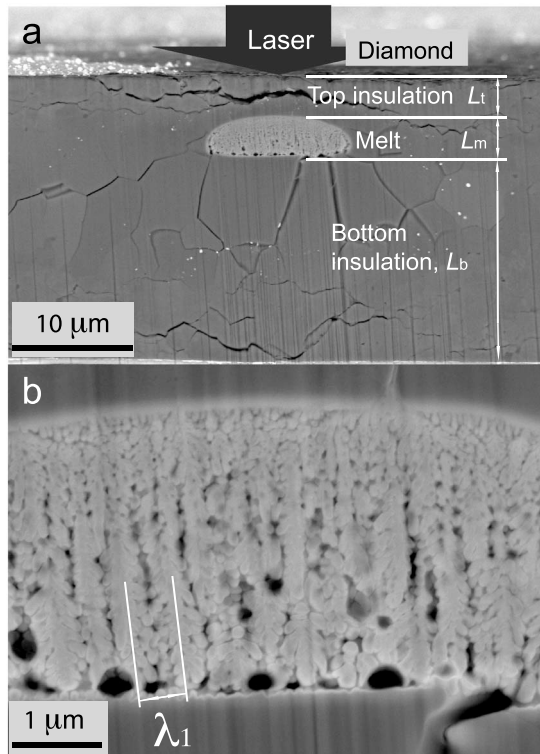


Figure 1. Microstructure of quenched (Mg, Fe)O melt from high pressures. (a) Cross section of quenched (Mg, Fe)O sample (14-0409-91) from 3 GPa and a peak temperature of 2830 (± 250) K (Du & Lee, 2014). The top and bottom insulation layer thicknesses are labeled, as is the Fe-rich melt region, L_t , L_m , and L_b , respectively. Below the melt bleb, large grains ($\sim 10 \mu\text{m}$) of Fe-depleted (Mg, Fe)O are also visible. Note that samples are heated by a single laser from the top. (b) Zoomed in view of dendritic features shown in melt bleb. Primary dendritic arm spacing λ_1 is labeled. Dendrites begin to grow from the top surface and grow toward the bottom surface.

As follows, we discuss two approaches to estimate D and, subsequently, to calculate η from the Eyring relation.

3. Estimating D

3.1. Approach I: Dendrite Growth Model

In the first approach to determine D and the resulting η , we use the dendritic growth model (Kurz & Fisher, 1981), as follows:

$$\lambda_1 = 4.3(\Gamma\Delta T D/k)^{0.25} G^{-0.5} V^{-0.25} \quad (2)$$

Solving for D , we have

$$D = (\lambda_1/4.3)^4 G^2 V k (\Gamma\Delta T)^{-1} \quad (3)$$

where λ_1 is the primary dendritic arm spacing (Figure 1b), G is the temperature gradient in front of the liquidus isotherm, V is growth rate of the dendrites, k is partition coefficient of solute, (i.e., Fe in this study), Γ is Gibbs-Thomson coefficient, and ΔT is the temperature difference between the liquidus and solidus equilibrium temperatures at the melt composition. The Gibbs-Thomson coefficient Γ of (Mg, Fe)O system is estimated at $\sim 10^{-7}$ K m at our experimental conditions, listed in Table 3, and plotted in Figure S1 (see details in supporting information).

As it is shown in Figure 1a, the top insulation layer (note that the sample insulates itself; L_t is $\sim 1-3 \mu\text{m}$) is much thinner than the bottom insulation layer L_b (Table 2). So the cooling of the melt layer is mostly through the top, very thin insulation layer. Due to the temperature dependence of thermal diffusivity of the sample κ (e.g., Stackhouse et al., 2010), the effective thickness of this insulation is much smaller, estimated as one fourth of the actual thickness, $\frac{L_t}{4}$, that is, $0.25-0.75 \mu\text{m}$. Therefore, the time scale of cooling this top insulation is $(L_t/4)^2/\kappa < 0.5 \mu\text{s}$, where κ is taken at the highest temperature (Table 2). The time scale of cooling of the melt layer is controlled by the quenching rate of the laser, that is, the laser fall time, and the thermal conduction of the melt layer itself. Laser fall time is estimated

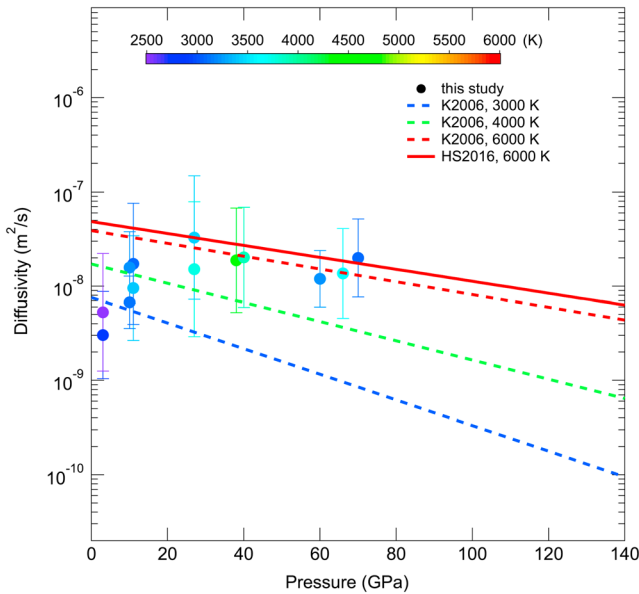


Figure 2. Diffusivity of (Mg, Fe)O melt at liquidus temperature at high pressures. Red solid lines are for (Mg_{0.75}Fe_{0.25})O at 6000 K (HS2016) (Holmstrom & Stixrude, 2016). Red, green, and blue dashed lines are for MgO at 6000 K, 4000 K, and 3000 K, respectively (K2006) (Karki et al., 2006). Our results are plotted as solid circles. These are determined by Approach I, except for the experiments “Jul0415” at 60 GPa and “13-1009” at 70 GPa which are determined by Approach II. Color represents the liquidus temperatures, as shown in color bar.

Uncertainties are given by the uneven thickness of the melt pocket (L_m). Dendritic growth is assumed to be controlled by the thermal cooling of the melt pocket; therefore, $V = L_m / \tau_m$. We also note that the estimated D likely represents the slowest species of the (Mg, Fe)O melt. Here we assume that all species, that is, Mg, Fe, and O, have similar self-diffusivities (Holmstrom & Stixrude, 2016), and therefore we approximate the estimated D as elemental self-diffusivity in order to calculate the viscosity using equation (1).

3.2. Approach II: Simple Model—Order of Magnitude Estimates

In the second approach, we estimate the viscosity of the melt that lacks clear dendritic features upon quench: experiments “13-1009” and “Jul0415” (Figure S4). This is likely due to shorter cooling times caused by thin insulation layers and thin melt layers (Table 2), as a consequence of higher pressures. The growth of crystals from molten (Mg, Fe)O during quenching is limited by chemical diffusion of the slowest species in the melt. Theoretical calculations show that diffusivities of Mg, Fe (both in high- and low-spin states), and O are fairly similar for (Mg, Fe)O liquid (Holmstrom & Stixrude, 2016). Therefore, we assume that the slowest species is Fe or Mg in this study as no other experimental studies are available for liquids of this composition. Crystal size (d) corresponds to the chemical diffusion length scale of $\sim (D\tau)^{1/2}$, and therefore $D \sim d^2/\tau$, where D is the self-diffusivity of Fe or Mg, and τ is the growth time of quenching crystals.

Additionally, using Approach II for samples with quenched dendritic texture yields values consistent with those attained through Approach I.

4. Results and Discussions

4.1. Diffusivity (D)

The calculated D from both approaches are listed in Table 3 and plotted in Figure 2. The uncertainties of D are given in Table 2, which are cumulative errors resulting from the measurements in our experiments and represent to what factor D is known (e.g., D is known to vary within a factor of 2.9 for experiment 14-049-91). For melt diffusivity and viscosity at low pressure (i.e., 3 GPa), our results are in good agreement with the computational results for MgO at 0 GPa (Alfe, 2005; Karki, 2015; Karki et al., 2013), within experimental and unknown computational uncertainties, thus validating our method (Figures 2 and 3).

by the time it takes for the laser power to drop by 20–30% of its peak power, which is $\sim 0.7 \mu\text{s}$ (Figure S2).

The cooling of the melt layer itself is estimated by the thermal diffusion time scale for the melt layer to cool: $\tau_m \sim (L_m)^2 / \kappa_m$, where L_m and κ_m are the thickness and thermal diffusivity of (Mg, Fe)O melt, respectively. L_m is $\sim 2 \mu\text{m}$ measured by the cross section of each recovered sample as shown in Figure 1a. κ_m is $\sim 1 \text{ mm}^2/\text{s}$ assumed as the same value of MgO solid near the melting temperature, where thermal diffusivity of MgO solid at various temperatures and pressures is taken from previous computational results (Stackhouse et al., 2010). Therefore, the time scale for the melt layer to cool is $\sim 4 \mu\text{s}$. This is much slower than cooling through the top insulation layer. As such, the cooling of the melt layer with time is controlled by the quenching rate of the laser, that is, laser fall time and the thermal conduction of the melt layer itself. These estimates are summarized in Table 3. A schematic of the temperature distribution along the compression axis for laser-heated diamond anvil cell melting sample during quenching is shown in Figure S3.

Partition coefficients k are determined from the MgO-FeO phase diagrams up to 66 GPa (Deng et al., 2017; Du & Lee, 2014). Average values are taken, with uncertainties indicating the range (Table 3). ΔT at each pressure is determined by taking the difference of liquidus and solidus temperature at melt composition. G is estimated as the difference in solidus and liquidus temperature at melt compositions divided by the thickness of the melt within melt pockets, which is $\sim \Delta T / L_m$.

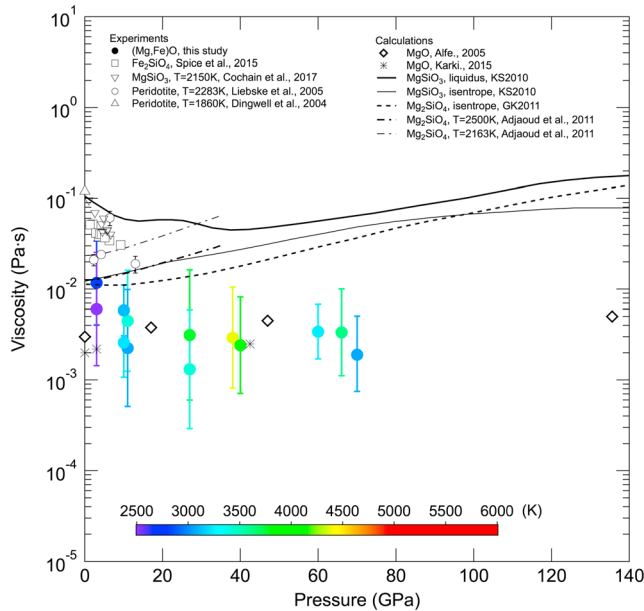


Figure 3. Viscosity at high pressures for relevant mantle compositions. Our melt viscosity results are for $(\text{Mg}_{1-x}\text{Fe}_x)\text{O}$ ($x = 0.25\text{--}0.6$) melt shown in solid circles, as error bars shown in solid lines determined by Approach I, except for experiments “Jul0415” at 60 GPa and “13-1009” at 70 GPa which are determined by Approach II. Temperatures are considered as liquidus temperatures at respective pressures. Note that our results are in reasonable agreement with computational results for MgO (stars; Karki, 2015) and (open diamonds; Alfe, 2005). Other computational results are also shown as solid lines for MgSiO_3 (Karki & Stixrude, 2010) and broken lines for Mg_2SiO_4 (Adjaoud et al., 2011). Previous experimental studies are shown as open circles for peridotite liquid at 2283 K up to 13 GPa (Liesbke et al., 2005), open triangle for peridotite liquid at 1830 K at 1 atm (Dingwell et al., 2004), open squares for fayalite melt at or above liquidus up to 9 GPa (Spice et al., 2015), and open inverted triangles for MgSiO_3 melt at ~ 2150 K up to 6.6 GPa (Cochain et al., 2017). Color represents the liquidus temperatures, as shown in color bar.

4.2. Viscosity

Using the Eyring relationship, we determine the viscosity of $(\text{Mg}, \text{Fe})\text{O}$ melts up to 70 GPa (Table 3 and Figure 3). The viscosity of $(\text{Mg}, \text{Fe})\text{O}$ at liquidus temperatures gradually decreases from 10 mPa s at 3 GPa to 1 mPa s at ~ 20 GPa and stays nearly constant up to 70 GPa. This apparent negative pressure dependence from 3 to 20 GPa is consistent with previous results on fayalite melt (Spice et al., 2015), likely due to the increase in Fe-O coordination with pressure (Sanloup et al., 2013).

4.3. Effect of Fe on Viscosity

In this study, the iron content, x , in $(\text{Mg}_{1-x}\text{Fe}_x)\text{O}$ melt ranges from 0.25 to 0.6. However, at the pressure and temperature range of our experiments, the viscosity of melt does not vary with Fe content within experimental uncertainties, as shown in Figure 3. This is consistent with the finding that diffusivities of $(\text{Mg}_{0.75}\text{Fe}_{0.25})\text{O}$ melt are fairly similar to MgO liquid, within a factor of 1.5 in the pressure and temperature range 0 to 200 GPa and 6000 K to 10000 K, respectively (Holmstrom & Stixrude, 2016). Therefore, it appears that the major difference between viscosity for $(\text{Mg}, \text{Fe})\text{O}$ and that for MgSiO_3 and Mg_2SiO_4 are most likely due to silicon concentration (Adjaoud et al., 2011; Ghosh & Karki, 2011; Karki & Stixrude, 2010) and/or the possible change of Fe-O coordination at high pressures (Sanloup et al., 2013).

4.4. Effect of Fe^{2+} Spin State in $(\text{Mg}, \text{Fe})\text{O}$ Melt

It is expected that Fe^{2+} in $(\text{Mg}, \text{Fe})\text{O}$ melt will go through a spin transition from high spin to low spin (Ghosh & Karki, 2016; Holmstrom & Stixrude, 2016). Also, it has been argued that the spin transition of the melt has a dramatic effect on Fe partitioning between solid and melt, causing a sudden Fe enrichment in silicate melt after ~ 70 GPa (Nomura et al., 2011). However, recent studies show that the spin transition of Fe^{2+} in Fe_2SiO_4 and $(\text{Mg}_{0.75}\text{Fe}_{0.25})\text{O}$ melt is gradual and broad over 200 GPa. As a result, most of the Fe^{2+} remains in high spin-up to CMB conditions, as there is much greater variety of Fe coordination

environments in liquids than solids (Ghosh & Karki, 2016; Holmstrom & Stixrude, 2016; Ramo & Stixrude, 2014). Particularly, it is found that self-diffusivities of $(\text{Mg}_{0.75}\text{Fe}_{0.25})\text{O}$ melt are fairly similar to MgO liquid (Holmstrom & Stixrude, 2016). Therefore, we suggest that this is also the case for $(\text{Mg}, \text{Fe})\text{O}$ melt and spin transition of Fe^{2+} is unlikely to have a significant effect on its viscosity up to the CMB.

4.5. Parameterization of Melt Viscosity

We parameterized viscosity η as follows (Ni et al., 2015):

$$\text{Log}_{10}\eta = a + b/T + cP/T \quad (4)$$

where P and T are pressure in gigapascals and liquidus temperature in kelvin, respectively, as well as fitting parameters a , b , and c . Applying multiple linear regressions with equation (4) to our data set (Table 2), it yields

$$\text{Log}_{10}\eta = -2.5 (0.5)$$

where standard errors are shown in parentheses. Parameters b and c are found to be statistically insignificant after applying an F test (P value > 0.05). Thus, viscosity of $(\text{Mg}, \text{Fe})\text{O}$ melt appears to be approximately a constant, similar to that of MgO predicted by previous computational studies (Alfe, 2005; Karki, 2015).

We calculate η at CMB conditions at present day, namely, 4000 K, 135 GPa (e.g., Boehler, 2000) to be $10^{-2.5(\pm 0.5)}$ Pa s. This is in excellent agreement with theoretical calculations for pure MgO melt at CMB pressures (Alfe, 2005) but $\sim 1\text{--}2$ orders of magnitude lower than MgSiO_3 and Mg_2SiO_4 melt (Adjaoud et al., 2011; Karki & Stixrude, 2010).

We note that the approach taken above to extrapolate our results to the CMB is crude. Several factors could affect our predicted viscosity at the CMB, including the following: there are other ways to parameterize viscosity besides equation (4) (Ni et al., 2015); the spin transition of Fe occurs in (Mg, Fe)O melt in the pressure range investigated (Ghosh & Karki, 2016; Holmstrom & Stixrude, 2016); and the temperature and pressure coefficient terms b and c cannot both be constrained in this study, due to the fact that the measurements are made along the melting curve and thus T and P are correlated. Therefore, when extrapolated, our results likely bear uncertainties associated with our factors mentioned above.

Given the possible drawbacks, our study is, nonetheless, the first experimental study to constrain viscosity of (Mg, Fe)O melt up to 70 GPa and demonstrates the feasibility of our new method using quenched textures. More studies are needed at higher pressures (> 70 GPa) and for various compositions (Fe, Si, Al, Ca, etc.) to understand the viscosity of partial melt throughout the lower mantle. These studies will provide a strong basis to understand melt migration processes and ultimately the nature and origin of ultralow-velocity zones (e.g., Lay et al., 2004; Williams & Garnero, 1996).

5. Geodynamical Implications: Magma Ocean

A deep magma ocean likely formed after the energetic Moon-forming giant impact (e.g., Canup & Asphaug, 2001; Cuk & Stewart, 2012). As the magma ocean is likely composed of multiple components, that is, (Mg, Fe)O and MgSiO_3 , we assume that the viscosity of the magma ocean lies in between these two end-member components (Shaw, 1972). Our results suggest that (Mg, Fe)O is lower than that of the MgSiO_3 at least up to 70 GPa. This reinforces the notion that the magma ocean is in the regime of turbulent convection with a Rayleigh number $Ra > 10^{30}$ (Karki & Stixrude, 2010). A simple model suggests that the lifetime of the magma ocean (t_{MO} , Myr) is primarily determined by its viscosity (η), which is $t_{\text{MO}} \sim 0.018 \eta^{3/7}$ and is rather short, that is, less than 20 kyr (Monteux et al., 2016). The presence of turbulence mixing may influence the settling of crystals during the cooling. As a result, this may affect the primary chemical differentiation after the magma ocean has solidified (Solomatov & Stevenson, 1993). More importantly, at lower mantle pressures, MgSiO_3 bridgmanite is expected to be the first phase to crystallize (e.g., Boukare et al., 2015; Nomura et al., 2011). Therefore, as the magma ocean crystallizes, the coexisting magma may become increasingly Si poor and therefore likely less viscous, as our results suggest. However, the exact melt composition is still poorly known (Boukare et al., 2015) and therefore the estimation of viscosity of a given magma ocean composition remains very uncertain. This may play a role in mixing of crystals and the magma ocean, although the critical physical processes are still not well understood (e.g., Boukare & Ricard, 2017; Solomatov & Stevenson, 1993).

6. Conclusions

We perform high-pressure melting experiments on (Mg, Fe)O up to 70 GPa. By analysis of the quenched textures after melting, we are able to estimate the elemental self-diffusion of (Mg, Fe)O melt from two independent approaches and show consistent results. Using the Eyring relation, we calculate the viscosity of the melt. We find that the viscosity of (Mg, Fe)O melt near liquidus temperatures is 10^{-3} – 10^{-2} Pa s and does not vary much over the pressure range of 3–70 GPa. We find that the viscosity of (Mg, Fe)O melt at the CMB is ~ 1 – 2 orders of magnitude lower than previous computational results for Si-rich melt at similar conditions while consistent with previous computational studies on MgO. Our results suggest turbulent convection and fast cooling of Earth's early magma ocean.

References

- Adjaoud, O., Steinle-Neumann, G., & Jahn, S. (2011). Transport properties of Mg_2SiO_4 liquid at high pressure: Physical state of a magma ocean. *Earth and Planetary Science Letters*, 312, 463–470. <https://doi.org/10.1016/j.epsl.2011.10.025>
- Alfe, D. (2005). Melting curve of MgO from first-principles simulations. *Physical Review Letters*, 94, 235701. <https://doi.org/10.1103/PhysRevLett.94.235701>
- Boehler, R. (2000). High-pressure experiments and the phase diagram of lower mantle and core materials. *Reviews of Geophysics*, 38(2), 221–245. <https://doi.org/10.1029/1998RG000053>
- Boukare, C. E., & Ricard, Y. (2017). Modeling phase separation and phase change for magma ocean solidification dynamics. *Geochemistry, Geophysics, Geosystems*, 18, 3385–3404.
- Boukare, C. E., Ricard, Y., & Fiquet, G. (2015). Thermodynamics of the MgO-FeO-SiO₂ system up to 140GPa: Application to the crystallization of Earth's magma ocean. *Journal of Geophysical Research: Solid Earth*, 120, 6085–6101. <https://doi.org/10.1002/2015JB011929>
- Canup, R. M. (2004). Dynamics of lunar formation. *Annual Review of Astronomy and Astrophysics*, 42, 441–475. <https://doi.org/10.1146/annurev.astro.41.082201.113457>

Acknowledgments

Data supporting Figures 2 and 3 are available in Tables 2 and 3 and supporting information. We thank L. Miyagi, D. Bercovici, J. Korenaga, S. Karato, R. Cohen, J. Wettlaufer, and S. Peppin for constructive discussions; M. Rooks and F. Camino for FIB help at YINQE Yale University and CFN at Brookhaven National Lab, respectively; Z. Jiang for SEM assistance; J. Eckert for EPMA measurements; and J. Girard, G. Amulele, W. Samela, and C. Fiederlein for technical support. We thank T. Pier of SPI Lasers and the support staff of National Instruments for assistance on LabVIEW programming. We also appreciate constructive comments from three anonymous reviewers. Facilities use was supported by YINQE and NSF MRSEC DMR 1119826. Research was carried out in part at the Center for Functional Nanomaterials, Brookhaven National Laboratory, which is supported by the U.S. Department of Energy, Office of Basic Energy Sciences, under contract DE-AC02-98CH10886. This work was funded in part by NSF (EAR-1551438, EAR-1321956, and EAR-0955824) and CDAC.

- Canup, R. M., & Asphaug, E. (2001). Origin of the Moon in a giant impact near the end of the Earth's formation. *Nature*, 412(6848), 708–712. <https://doi.org/10.1038/35089010>
- Cochain, B., Sanloup, C., Leroy, C., & Kono, Y. (2017). Viscosity of mafic magmas at high pressures. *Geophysical Research Letters*, 44, 818–826. <https://doi.org/10.1002/2016GL071600>
- Cuk, M., & Stewart, S. T. (2012). Making the Moon from a fast-spinning Earth: A giant impact followed by resonant despinning. *Science*, 338, 1047–1052. <https://doi.org/10.1126/science.1225542>
- Deng, J., Du, Z., Benedetti, L. R., & Lee, K. K. M. (2017). The influence of wavelength-dependent absorption and temperature gradients on temperature determination in laser-heated diamond-anvil cells. *Journal of Applied Physics*, 121(2), 11.
- Deng, J., & Lee, K. K. M. (2017). Viscosity jump in the lower mantle inferred from melting curves of ferropericlase. *Nature Communications*, 8, 1997. <http://doi.org/10.1038/s41467-017-02263-z>
- Dingwell, D. B., Courtial, P., Giordano, D., & Nichols, A. R. L. (2004). Viscosity of peridotite liquid. *Earth and Planetary Science Letters*, 226, 127–138. <https://doi.org/10.1016/j.epsl.2004.07.017>
- Du, Z., & Lee, K. K. M. (2014). High-pressure melting of MgO from (Mg, Fe)O solid solutions. *Geophysical Research Letters*, 41, 8061–8066. <https://doi.org/10.1002/2014GL061954>
- Elkins-Tanton, L. T. (2012). Magma oceans in the inner solar system. *Annual Review of Earth and Planetary Sciences*, 40, 113–139. <https://doi.org/10.1146/annurev-earth-042711-105503>
- Eyring, H. (1936). Viscosity, plasticity, and diffusion as examples of absolute reaction rates. *Journal of Chemical Physics*, 4(4), 283–291. <https://doi.org/10.1063/1.1749836>
- Ghosh, D. B., & Karki, B. B. (2011). Diffusion and viscosity of Mg₂SiO₄ liquid at high pressure from first-principles simulations. *Geochimica et Cosmochimica Acta*, 75, 4591–4600. <https://doi.org/10.1016/j.gca.2011.05.030>
- Ghosh, D. B., & Karki, B. B. (2016). Solid-liquid density and spin crossovers in (Mg, Fe)O system at deep mantle conditions. *Scientific Reports*, 6, 1997. <https://doi.org/10.1038/s41598-016-01997-2>
- Holmstrom, E., & Stixrude, L. (2016). Spin crossover in liquid (Mg, Fe)O at extreme conditions. *Physical Review B*, 93. <https://doi.org/10.1103/PhysRevB.93.195142>
- Kanzaki, M., Kurita, K., Fujii, T., Kato, T., Shimomura, O., & Akimoto, S. (1987). A new technique to measure the viscosity and density of silicate melts at high pressure. In M. Manghnani (Ed.), *High Pressure Research in Mineral Physics* (pp. 195–200). Washington, DC: Terapub/American Geophysical Union.
- Karki, B. B. (2015). First-principles computation of mantle materials in crystalline and amorphous phases. *Physics of the Earth and Planetary Interiors*, 240, 43–69. <https://doi.org/10.1016/j.pepi.2014.11.004>
- Karki, B. B., Bhattarai, D., & Stixrude, L. (2006). First-principles calculations of the structural, dynamical, and electronic properties of liquid MgO. *Physical Review B*, 73. <https://doi.org/10.1103/PhysRevB.73.174208>
- Karki, B. B., & Stixrude, L. P. (2010). Viscosity of MgSiO₃ liquid at Earth's mantle conditions: Implications for an early magma ocean. *Science*, 328, 740–742. <https://doi.org/10.1126/science.1188327>
- Karki, B. B., Zhang, J., & Stixrude, L. (2013). First principles viscosity and derived models for MgO-SiO₂ melt system at high temperature. *Geophysical Research Letters*, 40, 94–99. <https://doi.org/10.1029/2012GL054372>
- Kurz, W., & Fisher, D. J. (1981). Dendritic growth at the limit of stability: Tip radius and spacing. *Acta Metallurgica*, 29(1), 11–20. [https://doi.org/10.1016/0001-6160\(81\)90082-1](https://doi.org/10.1016/0001-6160(81)90082-1)
- Lay, T., Garnero, E. J., & Williams, Q. (2004). Partial melting in a thermo-chemical boundary layer at the base of the mantle. *Physics of the Earth and Planetary Interiors*, 146, 441–467. <https://doi.org/10.1016/j.pepi.2004.04.004>
- Li, J., & Agee, C. J. (1996). Geochemistry of mantle-core differentiation at high pressure. *Nature*, 381(6584), 686–689. <https://doi.org/10.1038/381686a0>
- Lieske, C., Schmickler, B., Terasaki, H., Poe, B. T., Suzuki, A., Funakoshi, K., ... Rubie, D. C. (2005). Viscosity of peridotite liquid up to 13 GPa: Implications for magma ocean viscosities. *Earth and Planetary Science Letters*, 240, 589–604. <https://doi.org/10.1016/j.epsl.2005.10.004>
- Monteux, J., Andrault, D., & Samuel, H. (2016). On the cooling of a deep terrestrial magma ocean. *Earth and Planetary Science Letters*, 448, 140–149. <https://doi.org/10.1016/j.epsl.2016.05.010>
- Ni, H., Hui, H., & Steinle-Neumann, G. (2015). Transport properties of silicate melts. *Reviews of Geophysics*, 53, 715–744. <https://doi.org/10.1002/2015RG000485>
- Nomura, R., Ozawa, H., Tateno, S., Hirose, K., Hernlund, J., Muto, S., ... Hiraoka, N. (2011). Spin crossover and iron-rich silicate melt in the Earth's deep mantle. *Nature*, 473(7346), 199–202. <https://doi.org/10.1038/nature09940>
- Ramo, D. M., & Stixrude, L. (2014). Spin crossover in Fe₂SiO₄ liquid at high pressure. *Geophysical Research Letters*, 41, 4512–4518. <https://doi.org/10.1002/2014GL060473>
- Rubie, D. C., Frost, D. J., Mann, U., Asahara, Y., Nimmo, F., Tsuno, K., ... Palme, H. (2011). Heterogeneous accretion, composition and core-mantle differentiation of the Earth. *Earth and Planetary Science Letters*, 301, 31–42. <https://doi.org/10.1016/j.epsl.2010.11.030>
- Sanloup, C., Drewitt, J. W. E., Creppis, C., Kono, Y., Park, C., McCammon, C., ... Bychkov, A. (2013). Structure and density of molten fayalite at high pressure. *Geochimica et Cosmochimica Acta*, 118, 118–128. <https://doi.org/10.1016/j.gca.2013.05.012>
- Shannon, R. D., & Prewitt, C. T. (1969). Effective ionic radii in oxides and fluorides. *Acta Crystallographica. Section B*, 25(5), 925–946. <https://doi.org/10.1107/S0567740869003220>
- Shaw, H. R. (1972). Viscosities of magmatic silicate liquids—Empirical method of prediction. *American Journal of Science*, 272(9), 870–893.
- Solomatov, V. S., & Stevenson, D. J. (1993). Suspension in convective layers and style of differentiation of a terrestrial magma ocean. *Journal of Geophysical Research*, 98, 5375–5390. <https://doi.org/10.1029/92JE02948>
- Spice, H., Sanloup, C., Cochain, B., de Grouchy, C., & Kono, Y. (2015). Viscosity of liquid fayalite up to 9 GPa. *Geochimica et Cosmochimica Acta*, 148, 219–227. <https://doi.org/10.1016/j.gca.2014.09.022>
- Stackhouse, S., Stixrude, L., & Karki, B. B. (2010). Thermal conductivity of Periclase (MgO) from first principles. *Physical Review Letters*, 104. <https://doi.org/10.1103/PhysRevLett.104.208501>
- Williams, Q., & Garnero, E. J. (1996). Seismic evidence for partial melt at the base of Earth's mantle. *Science*, 273(5281), 1528–1530. <https://doi.org/10.1126/science.273.5281.1528>
- Wood, B. J., Walter, M. J., & Wade, J. (2006). Accretion of the Earth and segregation of its core. *Nature*, 441, 825–833. <https://doi.org/10.1038/nature04763>

Geophysical Research Letters

Supporting Information for

Experimental constraints on viscosity of (Mg,Fe)O melt up to 70 GPa

Zhixue Du^{1*}, Jie Deng¹ and Kanani K. M. Lee¹

¹ Department of Geology & Geophysics, Yale University, New Haven, CT

* corresponding author, now at Geophysical Laboratory, Carnegie Institution of Washington

Contents of this file

Text S1
Figures S1 to S4

Introduction

This data set includes the details for the calculation of the Gibbs-Thomson coefficient (Γ). Figures are listed as Figs. S1-4, which describes calculated Gibbs-Thomson coefficient (Fig. S1), Laser modulation fall time (Fig. S2), Schematic of temperature distribution (Fig. S3), and Cross-section of quenched sample 13-009 (Fig. S4).

Text S1

Gibbs-Thomson coefficient Γ is defined as

$$\Gamma = \frac{\gamma_{SL}}{\Delta S_m},$$

where γ_{SL} is the solid-liquid interfacial energy and ΔS_m is the entropy of fusion per unit volume. γ_{SL} can be approximated by the empirical relationship proposed by [Turnbull, 1950],

$$\gamma_{SL} = \frac{\tau \Delta H_m}{(V_{molar}^s)^{2/3} N_A^{1/3}},$$

where the coefficient τ was found to be 0.34 for non-metallic systems. ΔH_m is the enthalpy of fusion, V_{molar}^s is the molar volume of solid phase and N_A is Avogadro's constant. Combining the above two equations yields,

$$\Gamma = \tau T_m \left(\frac{V_{molar}^s}{N_A} \right)^{1/3},$$

where T_m is the melting temperature. We calculate Γ of the endmembers, MgO and FeO, at various pressures and plot them in the Figure S1. The thermodynamic properties T_m and V_{molar}^s for MgO and FeO are calculated using the self-contained thermodynamic models by [Liebske and Frost, 2012] and [Komabayashi, 2014] respectively. For Γ of (Mg,Fe)O melt, T_m are the melting temperatures measured in this study and V_{molar}^s is calculated assuming an ideal mixing between MgO and FeO [Du and Lee, 2014]. Note that Γ for the (Mg,Fe)O melt at 60 and 70 GPa are not shown. Fast cooling leads to the lack of dendrite texture at those pressures. Therefore we employ Approach II to estimate D and η , which does not require the value of Γ .

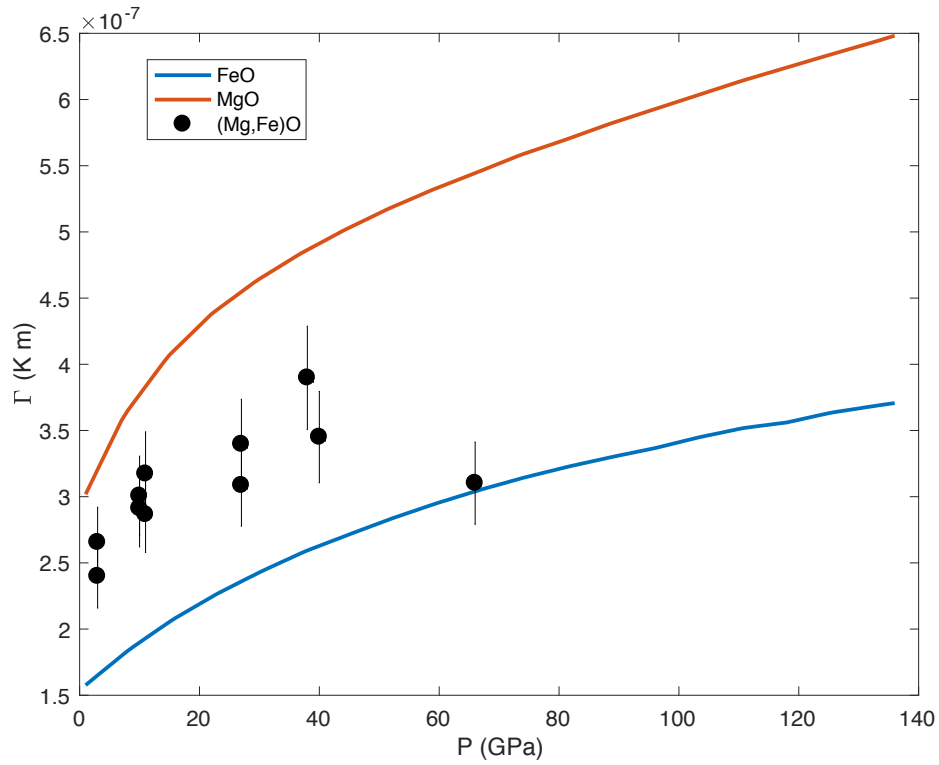


Figure S1. Calculated Gibbs-Thomson coefficient (Γ) at melting temperatures as a function of pressures. Results of this study at experimental conditions are shown as black filled circles, with 1σ error bar. For comparison, end-member MgO and FeO are shown in red and blue curves, respectively. Note that Γ for the (Mg,Fe)O melt for experimental no. Jul0415 (60 GPa) and 13-1009 (70 GPa) are not shown due to lack of dendrites.

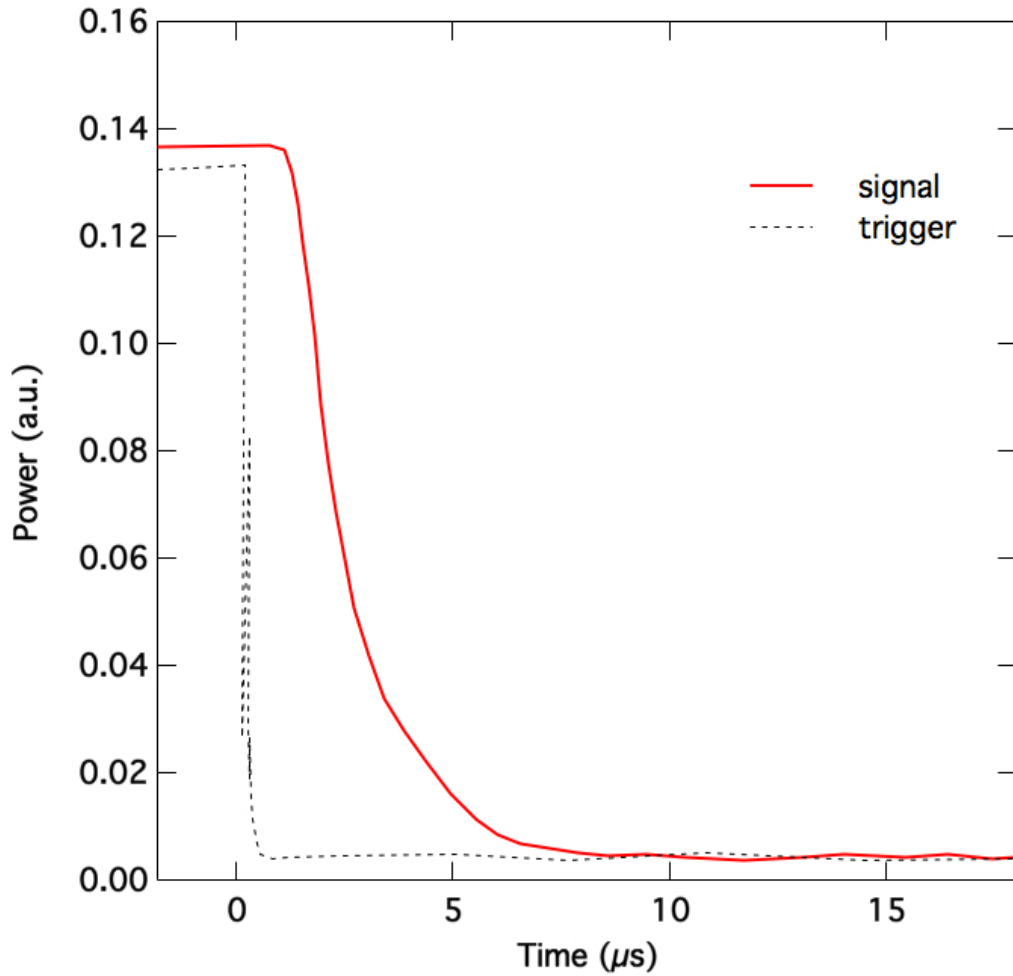


Figure S2. Laser modulation fall time. Thin red curve: trigger of laser modulation. Thick solid curve: signal of laser modulation. This figure is adapted from the manual of the SPI laser at 5kHz, 50% duty cycle, 100 W. Note that it takes $\sim 0.7 \mu\text{s}$ for the laser to fall in power by about 20%. As laser power tends to scale linearly with temperature (e.g., [Hirose *et al.*, 1999; Shen and Lazor, 1995]), we estimate that the difference between the liquidus and solidus temperatures would require a drop of $\sim 20\%$ laser power (i.e., 5000 K liquidus vs. 4000 K solidus).

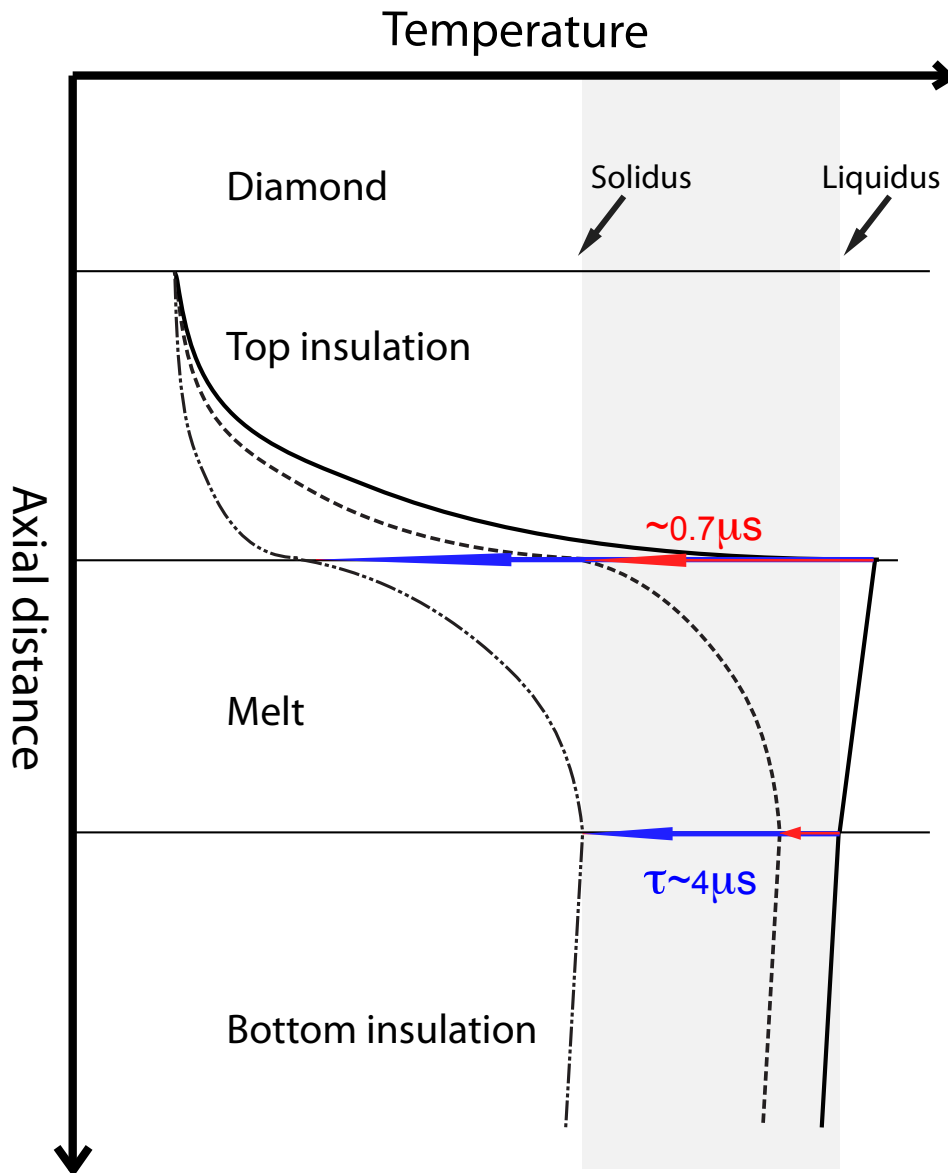


Figure S3. Schematic of temperature distribution along compression axis for LHDAC melting sample just prior to laser quench (solid curve), on laser quench (dashed curve) and just after laser quench (dash-dot curve). Red arrows show a time estimate of how long it takes the top surface of the melt bleb to cool from the super-liquidus to the solidus temperature, estimated from laser modulation time $\sim 0.7 \mu\text{s}$ in Fig. S1. Blue arrows show a time estimate of how long it takes the bottom surface of the melt bleb to cool from the liquidus to solidus temperature. Both sets of colored arrows show the difference in cooling between the top and bottom surfaces of the melt bleb due to differing thicknesses of thermal insulation. Note that since the bottom insulation is much thicker than the top, it takes longer for the bottom side to cool leaving larger dendritic features in the melt and larger coexisting solid grains on the bottom side of the melt (Fig.1a).

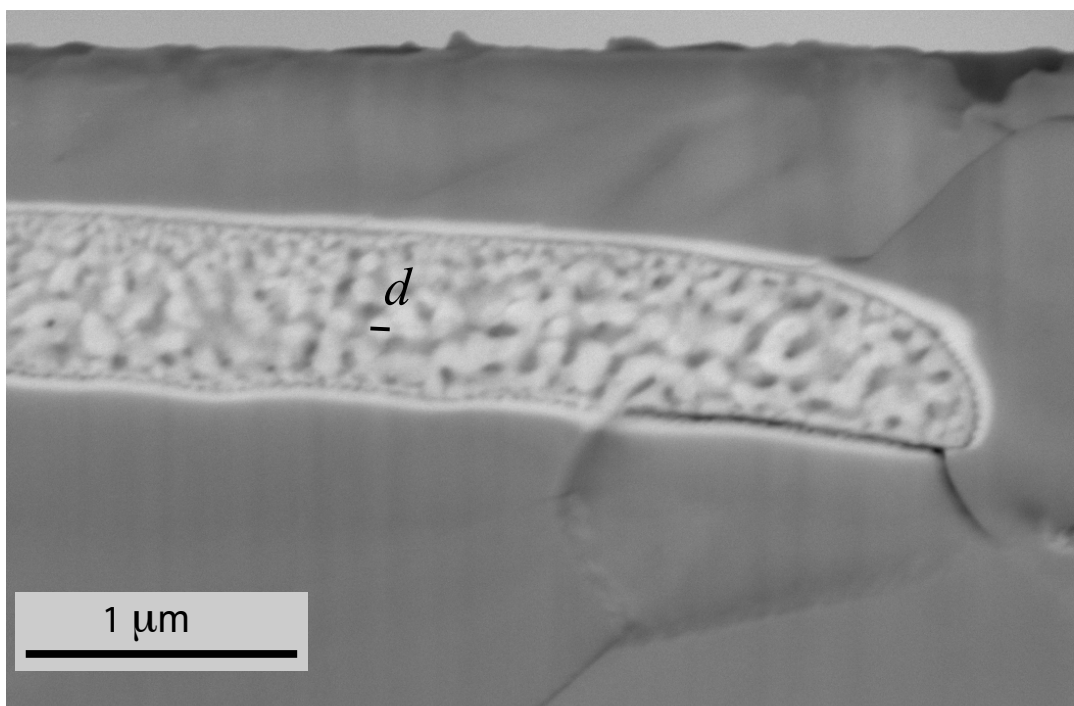


Figure S4. Cross-section of quenched (Mg,Fe)O sample (No. 13-1009) from 70 GPa and a peak temperature of 3100 K. Grain size (d) is shown as the black solid line as an example.